

# *Numerical investigations of reactive pollutant dispersion and personal exposure in 3D urban-like models*

Article

Accepted Version

Creative Commons: Attribution-Noncommercial-No Derivative Works 4.0

Zhang, Y., Yang, X., Yang, H., Zhang, K., Wang, X., Hang, J., Luo, Z. ORCID: <https://orcid.org/0000-0002-2082-3958> and Zhou, S. (2020) Numerical investigations of reactive pollutant dispersion and personal exposure in 3D urban-like models. *Building and Environment*, 169. 106569. ISSN 0360-1323 doi: 10.1016/j.buildenv.2019.106569 Available at <https://centaur.reading.ac.uk/87490/>

It is advisable to refer to the publisher's version if you intend to cite from the work. See [Guidance on citing](#).

To link to this article DOI: <http://dx.doi.org/10.1016/j.buildenv.2019.106569>

Publisher: Elsevier

All outputs in CentAUR are protected by Intellectual Property Rights law, including copyright law. Copyright and IPR is retained by the creators or other copyright holders. Terms and conditions for use of this material are defined in the [End User Agreement](#).

[www.reading.ac.uk/centaur](http://www.reading.ac.uk/centaur)

**CentAUR**

Central Archive at the University of Reading

Reading's research outputs online

1 To be submitted to Building and Environment 2019

2

3 Numerical investigations of reactive pollutant  
4 dispersion and personal exposure in 3D urban-like models

5

6 **Yong Zhang<sup>1</sup>, Xia Yang<sup>1</sup>, Hongyu Yang<sup>1</sup>, Keer Zhang<sup>1</sup>, Xuemei Wang<sup>2</sup>, Zhiwen  
7 Luo<sup>3</sup>, Jian Hang<sup>1,4\*</sup>, Shengzhen Zhou<sup>1\*</sup>**

8

9 <sup>1</sup>School of Atmospheric Sciences, Guangdong Province Key Laboratory for Climate  
10 Change and Natural Disaster Studies, Sun Yat-sen University, Guangzhou, P.R. China

11 <sup>2</sup>Institute for Environmental and Climate Research, Jinan University, Guangzhou, P. R.  
12 China

13 <sup>3</sup>School of the Built Environment, University of Reading, UK

14 <sup>4</sup>National Supercomputer center in Guangzhou, P.R. China

15

16 \*Corresponding author: Jian Hang, Shengzhen Zhou

17 Tel: +86-13710248541; +86-13710952752

18 E-mail address: hangj3@mail.sysu.edu.cn; zhouszh3@mail.sysu.edu.cn

19

20 **Abstract**

21 With satisfactory validation by experimental data, we perform computational  
22 fluid dynamic(CFD) simulations with the standard  $k-\varepsilon$  model to investigate how  
23 NO-NO<sub>2</sub>-O<sub>3</sub> photochemistry and turbulent mixing influence reactive pollutant  
24 dispersion and vehicular NO<sub>x</sub> exposure in 21-row(neighborhood-scale~1km)  
25 three-dimensional(3D) medium-dense urban models with an approaching wind  
26 parallel(perpendicular) to the main(secondary) streets. Personal intake fraction  $P_{iF}$   
27 and its spatially-averaged values for the entire building (i.e. building intake fraction  
28  $\langle P_{iF} \rangle_B$ ) are adopted for reactive/passive exposure analysis with/without  
29 NO<sub>x</sub>-O<sub>3</sub>-photochemistry.

30 Some meaningful findings are proposed: 1) There are flow adjustment processes  
31 coupling turbulent mixing and chemical reactions through urban areas(i.e. secondary  
32 Street 1 to 20). NO-NO<sub>2</sub>-O<sub>3</sub> photochemistry induces O<sub>3</sub> depletion and NO conversion  
33 into NO<sub>2</sub> producing significant increase in NO<sub>2</sub> exposure and slight decrease in NO  
34 exposure compared with passive dispersion. 2) With span-wise NO<sub>x</sub> sources, Street 10  
35 in the fully-developed region experiences weaker wind and subsequently greater  
36  $\langle P_{iF} \rangle_B$ (0.207ppm) than Street 3(0.135ppm) in the upstream flow-adjustment region.  
37  $\langle P_{iF} \rangle_B$  descends exponentially from the target building toward downstream, and  
38 Street 10 experiences quicker decay rates. 3) With stream-wise NO<sub>x</sub> sources along the  
39 main street,  $\langle P_{iF} \rangle_B$  first ascends, then reaches equilibrium values  
40 (e.g.0.046-0.049ppm for passive). 4) If background O<sub>3</sub> concentration [O<sub>3</sub>] rises from  
41 20ppbv to 40 and 100ppbv, more NO is oxidized by O<sub>3</sub> to generate NO<sub>2</sub>. As  
42 [O<sub>3</sub>]=20ppbv, if NO-NO<sub>2</sub> emission ratio decreases from 10 to 5, NO<sub>2</sub> exposure is

43 partly offset but NO exposure change little. Present methodologies are confirmed  
44 effective to investigate impacts of more complicated meteorological conditions and  
45 chemical mechanisms on exposure in urban districts.

46

47 **Keywords:** NO-NO<sub>2</sub>-O<sub>3</sub> photochemistry; reactive pollutant dispersion; personal  
48 intake fraction ( $P_{iF}$ ); building intake fraction ( $\langle P_{iF} \rangle_B$ ); computational fluid  
49 dynamic (CFD) simulation; three-dimensional (3D) urban models

50

## 51 **1. Introduction**

52 Following the ongoing urbanization worldwide, vehicular pollutant emissions  
53 have become one of the major sources in urban air pollution[1-3]. Heavy traffic flows,  
54 compact urban configurations and unfavorable meteorological conditions are the main  
55 reasons of large pollutant exposure and adverse health impacts on city dwellers[4]. On  
56 average, people spend more than 90% of their time indoors. Outdoor air pollutants in  
57 urban areas can penetrate into indoor via doors, windows, building cracks and other  
58 ventilation duct systems[5-7]. Particularly, vehicular pollutant exposure to urban  
59 residents living near busy roads should be paid more attention, because they suffer  
60 from higher health risks than other urban microenvironments[7-10]. Apart from  
61 reducing vehicular pollutant emissions, sustainable urban design with better  
62 understanding the influence of urban layouts and atmospheric conditions on the flow  
63 and passive/reactive pollutant dispersion in urban areas can help enhancing pollutant

64 dilution and mitigating traffic-related pollutant exposure[11-15].

65 As reviewed by the literature[16-29], in the past decades, a number of  
66 computational fluid dynamic (CFD) simulations, outdoor field observations and wind  
67 tunnel experiments have been widely performed to clarify turbulent flow  
68 characteristics and pollutant dispersion in urban models from street-scale (~100m) to  
69 neighborhood-scale (~1km). Street aspect ratios ( $H/W$ ) are reported as the most key  
70 urban parameters in two-dimensional (2D) street canyons[16-18, 25-26, 29-32].  
71 Realistic urban districts are usually three-dimensional (3D) with pollutant exchange  
72 across street roofs and lateral/stream-wise urban boundaries. Generally, the building  
73 planar area index  $\lambda_p$  (i.e. the ratio between the planar area of buildings viewed from  
74 above and the total floor area) and the frontal area index  $\lambda_f$  (i.e. the ratio of the frontal  
75 area of buildings to the total floor area) are typical building packing density indexes  
76 and key parameters of 3D urban areas[33-38]. Moreover, other significant factors  
77 have been also verified, such as building height variations[38-40], ambient wind  
78 directions[40-41], elevated building design[42-44], tree planting[46-49] etc. In  
79 addition, thermal stratification and buoyancy forces induced by wall heating and solar  
80 shading also significantly influence or dominate the flow and pollutant dispersion if  
81 wind speed is relatively small and Richardson number is large[50-56].

82 Recently, several researches[7, 44, 57] introduce personal intake fraction ( $P_{iF}$ )  
83 to quantify street-scale pollutant exposure induced by vehicle emissions. In contrast to  
84 population intake fraction ( $IF$ ) for a specific population[4, 58],  $P_{iF}$  is independent of  
85 population density and size which represents the fraction of pollutants inhaled

86 averagely by each person of a population to the total pollutant emissions. For example,  
87 1ppm (part per million or  $10^{-6}$ ) means the inhalation of 1mg pollutants if 1kg  
88 pollutants being emitted. By performing CFD simulations validated by experimental  
89 data, [Hang et al.\[7\]](#) estimated spatial mean  $P_{iF}$  (i.e.  $\langle P_{iF} \rangle \sim 1-5\text{ppm}$ ) of passive  
90 pollutant (i.e. CO) in shallow 2D street canyons ( $H/W=0.5-1$ ). Later,  $\langle P_{iF} \rangle$  in 3D  
91 urban district models were confirmed one order smaller ( $\sim 0.1\text{ppm}$ ) than 2D models  
92 with similar aspect ratios ( $H/W=0.5-1$ )[[41](#), [57](#)].

93 Besides the dynamic dispersion of passive pollutants, there are chemical  
94 processes of reactive pollutants in urban streets, such as the  $\text{NO}_x\text{-O}_3$  photochemistry  
95 [[59-64](#)],  $\text{NO}_x\text{-O}_3\text{-VOCs}$  chemical mechanisms[[65-69](#)] etc. Among them, the impacts  
96 of different heating scenarios and building configurations on reactive dispersion are  
97 extensively investigated through LES or RANS approaches, such as various shading  
98 settings[[61](#)], wall heating scenarios[[60](#), [62](#)], aspect ratios[[63](#)] etc. However, most  
99 studies so far mainly examine reactive pollutant dispersion in 2D street canyons while  
100 investigations on reactive pollutant dispersion and the related exposure in 3D urban  
101 models are still rare. Therefore, this study incorporates  $\text{NO-NO}_2\text{-O}_3$  chemistry into  
102 CFD simulations and numerically investigates reactive pollutant dispersion and  
103 exposure in urban models. As a start, the impacts of various ground-level source  
104 locations and reactant proportions ( $\text{NO:NO}_2\text{:O}_3$ ) in 3D medium-dense urban models  
105 ( $H/W=1$ ,  $\lambda_p=\lambda_f=0.25$ ) are studied under neutral meteorological conditions.

106 The sketch of this paper is organized as follows: Section [2](#) introduces the indexes  
107 for pollutant dispersion and exposure. Section [3](#) illustrates model setups and all test

108 cases in CFD simulations. Section 4 presents the flow and pollutant dispersion  
109 validations by wind tunnel data. Section 5 shows results and discussions, and Section  
110 6 draws the conclusions.

111

## 112 2. Indexes for pollutant dispersion and exposure

### 113 2.1 Personal intake fraction ( $P_{iF}$ ) and building intake fraction ( $\langle P_{iF} \rangle_B$ )

114 Population intake fraction ( $IF$ ) and personal intake fraction ( $P_{iF}$ ) are effective  
115 indexes to quantify vehicular pollutant exposure in local streets or neighborhoods[41,  
116 44, 57]. Both exposure indexes are defined as Eq. (1):

$$117 \quad IF = \sum_i^N \sum_j^M P_i \times Br_{i,j} \times \Delta t_{i,j} \times Ce_j / \dot{m} \quad (1a)$$

$$118 \quad P_{iF} = IF / \sum_j^M P_i \quad (1b)$$

119 where,  $N$  and  $M$  are the number of age groups and microenvironments,  $P_i$  represents  
120 the population size for the age group  $i$ ,  $Br_{i,j}$  ( $m^3/s$ ) and  $\Delta t_{i,j}$  (s) are the average  
121 breathing rate and the individual time spent for the  $i$ th age group in the  $j$ th  
122 microenvironment,  $Ce_j$  ( $kg/m^3$ ) denotes pollutant concentration in microenvironment  $j$   
123 and  $\dot{m}$  (kg) means total emissions released from vehicles. It is worth mentioning that  
124  $P_{iF}$  is independent of pollutant release rates as well as population density and size,  
125 but can be influenced by building configurations, meteorological conditions and  
126 pollutant source settings etc.

127 According to the literature[4, 70-71], the population data are categorized into

128 three subgroups( $N=3$ , Fig. 1a): Children(21.2%), Adults(63.3%) and Elders(15.5%).  
 129 Moreover, the time activity patterns for each subgroup are divided into four  
 130 microenvironments( $M=4$ , Fig. 1b): indoors at home( $j=1$ ), other indoor locations( $j=2$ ),  
 131 in or near vehicles( $j=3$ ), and other outdoor locations( $j=4$ ). Table 1 lists activity time  
 132 patterns and breathing rates in each subgroup for indoors at home( $j=1$ ). In this study,  
 133 all present building models are supposed to residential type and only  $j=1$  (indoors at  
 134 home) is adopted to calculate  $P_{iF}$  [44, 57]. Especially, the area-averaged  $P_{iF}$  of the  
 135 building wall surface is denoted as wall intake fraction( $\langle P_{iF} \rangle_w$ ). The  
 136 spatially-averaged  $P_{iF}$  of the entire building surfaces is represented as building  
 137 intake fraction( $\langle P_{iF} \rangle_B$ ), which means the fraction of total traffic emissions inhaled  
 138 averagely by each person living in this roadside building.

139

## 140 2.2 Photostationary state defect ( $d_{ps}$ , unit: %)

141 Referring to previous researches[59-60], the photostationary state defect ( $d_{ps}$ ) is  
 142 an effective indicator to measure the departure degree from photochemical  
 143 equilibrium and can be expressed in the following form:

$$144 \quad d_{ps} = \left( \frac{k_I[\text{NO}][\text{O}_3]}{J_{\text{NO}_2}[\text{NO}_2]} - 1 \right) \times 100 \quad (2)$$

145 here,  $k_I[\text{NO}][\text{O}_3]$  and  $J_{\text{NO}_2}[\text{NO}_2]$  represent the depletion and generation rates of  
 146 ozone.  $d_{ps}$  is positive value if ozone depletion rate greater than its formation rate, and  
 147 vice versa. Especially,  $d_{ps}$  equals zero when chemical reactions reach equilibrium  
 148 state.

149

### 150 3. CFD setups and case descriptions

#### 151 3.1 Numerical approaches

152 With advances in computer technologies, CFD as a powerful modelling tool has  
153 been widely employed to reproduce turbulent flow structure as well as to predict  
154 pollutant dispersion and transport in urban districts. Though large eddy simulations  
155 (LES) have been confirmed to be more accurate in predicting turbulence than  
156 Reynolds-Averaged Navier-Stokes (RANS) models[27, 73-75], RANS approaches are  
157 still extensively used, since LES models require expensive computational expenses  
158 and have challenges in selecting sub-grid scale models and specifying appropriate  
159 boundary conditions. Moreover, among the RANS models (e.g. various  $k-\varepsilon$  and  $k-\omega$   
160 models), the standard  $k-\varepsilon$  model shows good agreements with experimental data and  
161 has been widely adopted[7-8, 37-38, 45, 57-58, 76-79], although it has limitations in  
162 predicting turbulent kinetic energy in strong-wind regions. Therefore, by considering  
163 model performance and computational loads, the standard  $k-\varepsilon$  model is selected to  
164 solve the steady-state isothermal flow field. The governing equations for the flow and  
165 turbulent quantities implemented are as below[80]:

166 The mass continuity equation:

$$167 \frac{\partial \bar{u}_j}{\partial x_j} = 0 \quad (3)$$

168 The momentum equation:

169 
$$\bar{u}_j \frac{\partial \bar{u}_i}{\partial x_j} = -\frac{1}{\rho} \frac{\partial \bar{p}}{\partial x_i} + \frac{\partial}{\partial x_j} \left( \nu \frac{\partial \bar{u}_i}{\partial x_j} - \overline{u_i' u_j'} \right) \quad (4)$$

170 The transport equations of turbulent kinetic energy ( $k$ ) and its dissipation rate ( $\varepsilon$ ):

171 
$$\bar{u}_i \frac{\partial k}{\partial x_i} = \frac{\partial}{\partial x_i} \left[ \left( \nu + \frac{\nu_t}{\sigma_k} \right) \frac{\partial k}{\partial x_i} \right] + P_k - \varepsilon \quad (5)$$

172 
$$\bar{u}_i \frac{\partial \varepsilon}{\partial x_i} = \frac{\partial}{\partial x_i} \left[ \left( \nu + \frac{\nu_t}{\sigma_\varepsilon} \right) \frac{\partial \varepsilon}{\partial x_i} \right] + C_{\varepsilon 1} \frac{\varepsilon}{k} P_k - C_{\varepsilon 2} \frac{\varepsilon^2}{k} \quad (6)$$

173 where,  $\bar{u}_j$  is mean velocity components ( $\bar{u}_j = \bar{u}, \bar{v}, \bar{w}$  as  $j=1, 2, 3$ );  $\nu$  and  $\nu_t = C_\mu \frac{k^2}{\varepsilon}$

174 ( $C_\mu=0.09$ ) represent the kinematic viscosity and the eddy viscosity, respectively; the

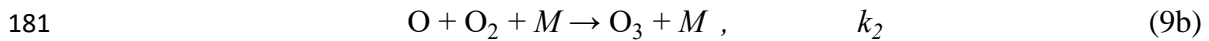
175 Reynolds stress tensor  $-\overline{u_i' u_j'}$  and the turbulence production term  $P_k$  are defined as:

176 
$$-\overline{u_i' u_j'} = \nu_t \left( \frac{\partial \bar{u}_i}{\partial x_j} + \frac{\partial \bar{u}_j}{\partial x_i} \right) - \frac{2}{3} k \delta_{ij} \quad (7)$$

177 
$$P_k = \nu_t \times \frac{\partial \bar{u}_i}{\partial x_j} \left( \frac{\partial \bar{u}_i}{\partial x_j} + \frac{\partial \bar{u}_j}{\partial x_i} \right) \quad (8)$$

178 Note that  $\delta_{ij}$  is the Kronecker delta whose value is 1 when  $i=j$  and otherwise is 0.

179 The NO<sub>x</sub>-O<sub>3</sub> simple photochemical mechanism is described as follows[59-60]:



183 Here,  $M$  denotes a third molecule, for example O<sub>2</sub> or N<sub>2</sub>, to absorb excess energy and

184 stabilize O<sub>3</sub> molecule formed;  $J_{\text{NO}_2}$ ,  $k_2$  and  $k_1$  represent rate constant for each

185 reaction, respectively. Since the oxygen atom (O) is highly reactive, it combines

186 rapidly with O<sub>2</sub> once O is produced from NO<sub>2</sub> photolysis. This is so-called

187 pseudo-steady-state approximation that the depletion and production rates of O<sub>3</sub> are

188 nearly equal[81]:

$$189 \quad k_2[\text{O}][\text{O}_2][\text{M}] = J_{\text{NO}_2}[\text{NO}_2] \quad (10)$$

190 Therefore, Eq. (9a) is the rate control step for O<sub>3</sub> formation. Based on the above  
191 assumption, the transport equations for reactive pollutants can be defined as[59-60]:

$$192 \quad \bar{u}_j \frac{\partial[\text{NO}]}{\partial x_j} = D_m \frac{\partial^2[\text{NO}]}{\partial x_j \partial x_j} + \frac{\partial}{\partial x_j} \left( D_e \frac{\partial[\text{NO}]}{\partial x_j} \right) + J_{\text{NO}_2}[\text{NO}_2] - k_I[\text{O}_3][\text{NO}] + S_{\text{NO}} \quad (11a)$$

$$193 \quad \bar{u}_j \frac{\partial[\text{NO}_2]}{\partial x_j} = D_m \frac{\partial^2[\text{NO}_2]}{\partial x_j \partial x_j} + \frac{\partial}{\partial x_j} \left( D_e \frac{\partial[\text{NO}_2]}{\partial x_j} \right) - J_{\text{NO}_2}[\text{NO}_2] + k_I[\text{O}_3][\text{NO}] + S_{\text{NO}_2} \quad (11b)$$

$$194 \quad \bar{u}_j \frac{\partial[\text{O}_3]}{\partial x_j} = D_m \frac{\partial^2[\text{O}_3]}{\partial x_j \partial x_j} + \frac{\partial}{\partial x_j} \left( D_e \frac{\partial[\text{O}_3]}{\partial x_j} \right) + J_{\text{NO}_2}[\text{NO}_2] - k_I[\text{O}_3][\text{NO}] \quad (11c)$$

195 where,  $D_m$  and  $D_e$  are the molecular and eddy diffusivity; the third terms on the  
196 right-hand side of Eq. (11) represent chemical reaction term;  $S_{\text{NO}}$  and  $S_{\text{NO}_2}$  denote the  
197 source terms of NO and NO<sub>2</sub>; the Schmidt number  $Sc_t = \nu_t / D_e$  is specified as 0.7[33, 39,  
198 46, 48, 78]. Furthermore, the photolysis rate  $J_{\text{NO}_2}$  and rate constant  $k_I$  are calculated by  
199 [59-60]:

$$200 \quad J_{\text{NO}_2} = 8.14 \times 10^{-3} \left\{ 0.97694 + 8.3700 \times 10^{-4} (T - 273.15) + 4.5173 \times 10^{-6} \times (T - 273.15)^2 \right\} \quad (12a)$$

201 )

$$202 \quad k_I = 4.405 \times 10^{-2} \exp\left(-\frac{1370}{T}\right) \quad (12b)$$

203 Here,  $T$  is temperature in K; the units of  $J_{\text{NO}_2}$  and  $k_I$  are s<sup>-1</sup> and ppbv<sup>-1</sup>s<sup>-1</sup>.

204 Additionally, the temperature-dependent rate constant is not considered in isothermal

205 flow of this study, thus  $J_{\text{NO}_2}$  and  $k_I$  are  $8.1 \times 10^{-3}$  s<sup>-1</sup> and  $4.450 \times 10^{-4}$  ppbv<sup>-1</sup>s<sup>-1</sup> by

206 assuming reactive pollutants undergo chemical processes under the isothermal

207 condition with a fixed  $T$  of 298.15K.

208 All governing equations(Eqs. (3-6, 11)) are discretized by a finite volume  
209 method (FVM) with the second-order upwind scheme. The SIMPLE algorithm is  
210 employed for pressure and velocity coupling. The under-relaxation factors for  
211 pressure, momentum,  $k$  and  $\varepsilon$  terms are specified as 0.3, 0.7, 0.8 and 0.8. Numerical  
212 simulation does not stop until the absolute residuals of all variables are less than  $10^{-6}$ .

213

### 214 **3.2 Three-dimensional (3D) urban model setups in CFD**

215 The building layouts, as depicted in Fig. 2a, are based on the idealized 3D  
216 medium-dense urban clusters (i.e. street aspect ratio  $H/W=1$ ; building packing density  
217  $\lambda_p=\lambda_f=0.25$ ). To better illustrate model configurations,  $x$ ,  $y$  and  $z$  are described as the  
218 stream-wise, span-wise and vertical directions, respectively. The cubic building  
219 models( $H=B=30\text{m}$ ) with a uniform spacing( $W_s=W_m=30\text{m}$ ) are constructed in  $x$  and  $y$   
220 directions. Moreover, the approaching wind is parallel to the main streets( $x$  direction)  
221 and perpendicular to the secondary streets( $y$  direction).  $x/H=0$  means the cross section  
222 in windward street opening and  $y/H=0$  denotes the central cross section of the main  
223 street (Fig. 2c).

224 As verified by the literature[38-40, 82-83], the airflow in the middle column is  
225 hardly affected by lateral boundaries if the lateral width of the urban model is  
226 sufficiently large. Hence, only half of the middle column with two lateral symmetry  
227 boundaries are considered during CFD simulations to reduce computational efforts  
228 (Fig. 2b). Following the CFD guidelines[84-86], the distances between urban

229 boundaries and the domain top, domain inlet, domain outlet are  $9H$ ,  $6.7H$  and  $32.3H$ ,  
 230 respectively. Furthermore, the zero normal gradient boundary condition is adopted at  
 231 two lateral boundaries and the domain top (i.e. symmetry) and the domain outlet (i.e.  
 232 outflow). Several recent studies[5-6, 8-9, 44, 57-58] reported that, pollutant  
 233 concentration on the wall surfaces of near-road buildings can be treated as indoor  
 234 concentration originated from outdoor pollutants since the indoor/outdoor (I/O) ratio  
 235 of pollutant concentration is nearly one for naturally-ventilated buildings[5, 72].  
 236 Therefore, by assuming all present building models are naturally-ventilated type, the  
 237 flow and pollutant dispersion within indoor space of buildings are not taken into  
 238 account to reduce the grid numbers and computational costs in CFD simulations. The  
 239 literature have applied such technique to effectively quantify vehicular pollutant  
 240 exposure in 2D street canyons or 3D urban models[5-6, 8-9, 44, 57-58].

241 For the domain inlet, the power-law time-averaged velocity profile  $U_0(z)$  in the  
 242 upstream free flow is adopted (Eq. 13a)[40-41, 57, 82-83] which is scaled to that in  
 243 wind tunnel experiments[87]. Base on the CFD guideline[84-86], vertical profiles of  
 244  $k(z)$  and  $\varepsilon(z)$  are given by Eqs. (13b-c):

$$245 \quad U_0(z) = U_{ref} \times (z/H)^{0.16} \quad (13a)$$

$$246 \quad k(z) = u_*^2 / \sqrt{C_\mu} \quad (13b)$$

$$247 \quad \varepsilon(z) = C_\mu^{3/4} k^{3/2} / (\kappa_\nu z) \quad (13c)$$

248 where,  $U_{ref}$  is the reference velocity at the building height in upstream free flow  
 249 ( $U_{ref}=3.0$  m/s at  $z = H$ ); the friction velocity  $u_*=0.24$ m/s[40-41, 57, 82-83]; von

250 Karman constant  $\kappa_v=0.41$ ,  $C_\mu=0.09$ . Furthermore, vertical profiles of Eq. (13)  
251 represent neutral atmospheric boundary layer with a full-scale surface roughness  
252  $z_0=0.1\text{m}$ [93] and have been adopted in previous studies[40-41, 57, 82-83].

253 In addition, Fig. 2c demonstrates the overhead and lateral views of mesh  
254 distribution for test cases. The minimum grid size of 0.2 m near the wall surfaces and  
255 the stretching ratio between adjacent grids of 1.15 (about 3.2 million hexahedral cells)  
256 are applied to ensure sufficiently fine grid at the pedestrian level (0-1.5m) and near  
257 building surfaces. As the normalized distance  $y^+$  ( $y^+=yu_\tau/\nu$ ) ranges from 30 to 600 at  
258 most regions of wall surfaces, standard wall function with no slip boundary condition  
259 is set on all wall surfaces. According to the literature[13, 40, 88-89], a specific  
260 roughness modification is assigned to the upstream and downstream ground to obtain  
261 a horizontally homogeneous ABL surrounding urban regions. Especially, the grid  
262 independence tests are presented later in subsection 4.1.

263

### 264 3.3 Pollutant source settings and model description of test cases

265 Three kinds of pollutant source locations are considered in this study, i.e. the  
266 span-wise (y direction) emission sources in the 3<sup>rd</sup> or 10<sup>th</sup> secondary street is denoted  
267 as S3 and S10 (Fig. 3a-b), and the stream-wise (x direction) emission sources along  
268 the main street is represented by Sm (Fig. 3c). The reactive pollutants involved in  
269 present photochemistry are NO, NO<sub>2</sub> and O<sub>3</sub>. Among them, NO<sub>x</sub> is assumed to be  
270 emitted from vehicles into the street canyon while background O<sub>3</sub> concentration is

271 specified at the domain inlet and entrained by approaching wind into urban districts.  
272 The background concentrations for NO and NO<sub>2</sub> at the domain inlet are zero in this  
273 study. Following the literature[59-60], typical automobile emission ratio of NO to  
274 NO<sub>2</sub> ( $R_{\text{NO}/\text{NO}_2}$ ) of 10 is adopted. NO and NO<sub>2</sub> are released from the lowest grid cell  
275 ( $z=0-0.2\text{m}$ ) at rates of 100 and 10 ppbv s<sup>-1</sup>, which corresponds to emission strengths  
276 of  $1.227\times 10^{-7}$  and  $1.88\times 10^{-8}$  kg m<sup>-3</sup>s<sup>-1</sup> ( $P=1$  atm,  $T=298.15\text{K}$ ). For S3 or S10 sources,  
277 as the street width ( $W_s$ ) is 30m, this NO<sub>x</sub> emission intensity of 849 μg m<sup>-1</sup>s<sup>-1</sup> is  
278 equivalent to a traffic volume of about 6100 vehicles per hour when considering a  
279 NO<sub>x</sub> emission of 0.5g km<sup>-1</sup> per vehicle[59-60]. Particularly, we are mainly concerned  
280 with the proportion among NO and NO<sub>2</sub> rather than the assigned emission rate for  
281 each vehicular pollutant.

282 Furthermore, four O<sub>3</sub> background concentrations (i.e. [O<sub>3</sub>] =1, 20, 40 and 100  
283 ppbv) with  $R_{\text{NO}/\text{NO}_2}=100:10$  are investigated to study the effects of different [O<sub>3</sub>] on  
284 reactive dispersion. In addition, Carslaw[90] verified that there is an increasing  
285 NO<sub>2</sub>/NO<sub>x</sub> emission ratio in road traffic emissions referring to observation in real cities.  
286 Thus, three emission ratios of NO to NO<sub>2</sub> (i.e.  $R_{\text{NO}/\text{NO}_2}=100:10$ , 50:10 and 100:20)  
287 with [O<sub>3</sub>]=20ppbv are considered to examine the impacts of various  $R_{\text{NO}/\text{NO}_2}$  on  
288 reactive pollutant dispersion.

289 Overall, total 11 test cases are described as Case P [Source,  $R_{\text{NO}/\text{NO}_2}$ ] or Case R  
290 [Source,  $R_{\text{NO}/\text{NO}_2}$ , [O<sub>3</sub>]] and summarized in Table 2. Here ‘P’ means passive dispersion  
291 without chemical reactions, ‘R’ denotes reactive dispersion with NO-NO<sub>2</sub>-O<sub>3</sub>  
292 chemistry; ‘Source’ contains three pollutant source locations, i.e. S3, S10 and Sm,

293 respectively;  $R_{\text{NO/NO}_2}$  represents the emission ratios of NO to NO<sub>2</sub>; [O<sub>3</sub>] is  
294 background O<sub>3</sub> concentration (mole fraction, unit: ppbv).

295

## 296 **4 Validation study of flow and pollutant dispersion in 3D urban models**

### 297 **4.1 Flow validation by wind tunnel data**

298 In this subsection, the performances of various steady  $k$ - $\varepsilon$  models (standard,  
299 RNG and Realizable) with standard wall function are evaluated by wind tunnel data.  
300 Moreover, the grid independence tests are also implemented.

301 As shown in Fig. 4a-b, idealized 3D urban models in wind tunnel experiment[87]  
302 consist of 7 rows and 11 columns of regularly-aligned cubic buildings  
303 ( $H=B=W=15\text{cm}$ ). Vertical profiles of velocity components ( $\bar{u}$ ,  $\bar{w}$ ) and turbulence  
304 kinetic energy ( $k$ ) are measured at points of  $V_i$  ( $i=1-6$ ), which are central positions in  
305 the  $i$ th secondary street located at  $y/H=1$  and  $x/H=1.5H, 3.5H, 5.5H, 7.5H, 9.5H,$   
306  $11.5H$  respectively (Fig. 4a-b).

307 In CFD validation study, the similar full-scale model configurations  
308 ( $H=B=W=30\text{m}$ , Fig. 4c) are reconstructed with the scale ratio of 200:1 to  
309 wind-tunnel-scale models. Moreover, all CFD setups including computational  
310 domains, boundary conditions and convergence criteria in this full-scale CFD  
311 validation study are similar with those in subsection 3.2 except that the distance  
312 between urban boundaries and domain outlet is  $40.3H$ (Fig. 4c). Based on the building  
313 height( $H=0.15\text{m}$  or  $30\text{m}$ ) and reference velocity( $U_{ref}=3\text{m/s}$ ), the reference Reynolds

314 number  $Re = \frac{U_{ref}H}{\nu} \approx 30000$  and  $6 \times 10^6$  for wind-tunnel-scale and full-scale urban  
315 models, which are much larger than 11000 satisfying Reynolds number independence  
316 requirement. Furthermore, Fig. 4d depicts the coarse, medium and fine grid  
317 arrangements with hexahedral cells of about 1, 2 and 3.3 million and the minimum  
318 grid size of 0.4m, 0.2m and 0.1m, respectively.

319 Fig. 5 first shows results of grid independence test at V1(Fig. 5a-b), then depicts  
320 vertical profiles of time-averaged stream-wise velocity  $\bar{u}(z)$  at Points V1, V4 and V6  
321 (Fig. 5c-e), vertical velocity  $\bar{w}(z)$  (Fig. 5f) and turbulence kinetic energy  $k(z)$  (Fig. 5g)  
322 at Point V1 between numerical results and experimental data. There is little difference  
323 in numerical results between the coarse, medium and fine grid, and thus medium grid  
324 is selected for case studies to reduce computational loads. Besides, the standard  $k-\varepsilon$   
325 model with the medium grid shows better agreements with wind tunnel data than the  
326 RNG and Realizable  $k-\varepsilon$  models.

327 To further quantify the modeling accuracy and reliability of the standard  $k-\varepsilon$   
328 model with the medium grid arrangement, several statistical performance metrics are  
329 applied, including the mean value, the standard deviation, the factor 2 (FAC2), the  
330 normalized mean square error (NMSE), the fraction bias (FB) and the correlation  
331 coefficient (R)[91]. Among which, the closer NMSE value to zero, the smaller  
332 difference between experiment data and CFD results; FAC2 value larger than one  
333 means over-prediction against experiment data while smaller than one represents  
334 under-prediction; Similarly, the negative and positive FB values denote  
335 overestimation and underestimation. Results of  $\bar{u}(z)$  at Points V1, V4 and V6 as well

336 as  $\bar{w}(z)$  and  $k(z)$  at Point V1 are listed in [Table 3](#). Referring to COST Action 732's  
337 recommended criteria[91], a credible CFD model should satisfy the following  
338 statistical metrics standards:  $0.5 \leq \text{FAC2} \leq 2$ ,  $\text{NMSE} \leq 1.5$  and  $-0.3 \leq \text{FB} \leq 0.3$ .  
339 Overall, metrics lie in the recommended criteria, particularly values of  $\bar{u}(z)$  meet  
340 well. However, values of  $\bar{w}(z)$  and  $k(z)$  reveal relatively poorer performance than  
341 those of  $\bar{u}(z)$ , which is largely attributed to the limitation of the standard  $k-\varepsilon$  model.  
342 Conclusively, the validation study shows that present CFD methodologies applying  
343 standard  $k-\varepsilon$  model with medium grid have credible numerical accuracy in predicting  
344 urban turbulent flow and can be employed for further case studies.

345

#### 346 **4.2 Validation of pollutant dispersion by wind tunnel data**

347 Experimental and numerical studies have been extensively performed to  
348 investigate passive pollutant dispersion in the idealized street canyons. Unfortunately,  
349 there are currently little experimental data to directly validate the present CFD model  
350 coupled with chemistry[59-60, 63-64]. However, the reactive pollutants considered in  
351 this paper are effectively passive and can be divided into two subsets, i.e. total  
352 nitrogen oxide ( $\text{NO}_x = \text{NO} + \text{NO}_2$ ) and total oxidant ( $\text{OX} = \text{NO}_2 + \text{O}_3$ ), since reactions ([Eq.](#)  
353 [9](#)) interconvert NO with  $\text{NO}_2$ , and  $\text{O}_3$  with  $\text{NO}_2$  but without redundant productions. In  
354 addition, the chemical reaction terms cancel out when [Eqs. \(11a-b\)](#) and [Eqs. \(11b-c\)](#)  
355 are added, which indicates that the transport and dispersion of  $\text{NO}_x$  and OX can be  
356 deemed as passive scalar. Consequently, in this subsection, Standard  $k-\varepsilon$  model with

357 standard wall function has been implemented and validated against wind tunnel  
358 experiment to evaluate the reliability of numerical simulation in predicting passive  
359 pollutant distribution.

360 The configurations of the wind tunnel measurement[92], as depicted in Fig.6a-b,  
361 are consisted of nine rectangular building models ( $L_x=27.6\text{cm}$ ,  $L_y=18.4\text{cm}$ ,  $H=8\text{cm}$ )  
362 with three rows and three columns ( $3\times 3$ ) and uniform street widths ( $W=8\text{cm}$ ,  $H/W=1$ ).  
363 Moreover, tracer gas( $\text{C}_2\text{H}_6$ ) is released from a line source (0.5cm in width,  $dx$  and  
364 18.4 cm in length,  $L_s$ ) at a velocity of  $w_{source}=0.01$  m/s which is paralleled with  $y$   
365 direction and locates in the central street canyon in front of building No.2(Fig. 6a-b).  
366 Furthermore,  $\text{C}_2\text{H}_6$  concentration profiles are measured in the middle of leeward and  
367 windward walls near the line source as well as on the central line of roof surface in  
368 the building No.2(Fig. 6a-b).

369 In full-scale pollutant dispersion validation study, similar model configurations  
370 ( $L_x=138\text{m}$ ,  $L_y=92\text{m}$ ,  $H=40\text{m}$ , in Fig. 6c) are rebuilt with the scale ratio of 500:1 to  
371 wind-tunnel-scale models. CFD setups are similar with subsection 3.2, but the  
372 distances between urban boundaries and the domain top, domain side, domain inlet,  
373 domain outlet are  $9H$ ,  $5H$ ,  $5H$  and  $15H$ , respectively. The approaching wind is parallel  
374 to the main streets( $x$  direction) and perpendicular to the secondary streets( $y$  direction).  
375 Furthermore, vertical profiles of stream-wise velocity  $\bar{u}(z)$ , turbulence kinetic energy  
376  $k(z)$  and turbulent dissipation rate  $\varepsilon(z)$  fitted by measured data in wind tunnel  
377 experiments[92] are adopted at the domain inlet (Fig. 6d-f). In addition, to compare  
378 CFD results with measured data, the normalized  $\text{C}_2\text{H}_6$  concentration  $K$  is defined as

379 below:

$$380 \quad K = CHU_{ref}/w_{source}dx \quad (14)$$

381 Here the height of building ( $H$ ), the reference velocity ( $U_{ref}$ ) and the line source  
382 emission strength ( $w_{source}, dx$ ) are applied.

383 As shown in Fig. 7, the agreements of  $K$  between wind tunnel data and CFD  
384 results are well confirming the standard  $k-\varepsilon$  model has sufficient modeling accuracy in  
385 predicting passive pollutant dispersion within 3D urban district models.

386

## 387 **5 Results and discussion**

### 388 **5.1 Flow patterns in 3D urban district models**

389 Fig. 8a depicts velocity distribution in the plane of  $z=1.5\text{m}$  (the pedestrian level).  
390 Obviously, the flow adjustment process can be observed through the entire building  
391 clusters, in which wind speed decreases toward downstream from Street 1 to Street 6,  
392 and then reaches a comparatively flow equilibrium from Street 7 to Street 18. Fig.  
393 8b-c further depict velocity magnitude and 2D streamlines in the plane of  $y=30\text{m}$  (the  
394 center plane of the target street canyon) and  $z=1.5\text{m}$  for Street 3 and Street 10.  
395 Moreover, the corresponding 3D streamlines are displayed in Fig. 8d. For both street  
396 units, 3D downward helical vortices are produced inside the secondary streets (Fig.  
397 8b-d). The lateral flow direction near street ground (i.e.  $z=1.5\text{m}$ ) are from the  
398 secondary streets to the main streets and from the downwind building (No.4 and 11)

399 to upwind building (No. 3 and 10) (Fig. 8c). In addition, Street 3 apparently  
400 experiences greater wind speed than Street 10.

401 In particular, the following analysis (subsection 5.3) emphasizes more on  
402 reactive pollutant dispersion in the fully-developed region (e.g. Street 10) than the  
403 flow-adjust region (e.g. Street 3).

404

## 405 **5.2 Impacts of source locations (S3, S10 and Sm) on reactive pollutant dispersion**

406 This subsection considers the impacts of source locations (i.e. S3, S10 and Sm in  
407 Fig. 3) on reactive pollutant dispersion (with chemical reactions, R-type) under the  
408 specific pollutant proportion (i.e.  $R_{\text{NO}/\text{NO}_2}=100:10$ ,  $[\text{O}_3]=20\text{ppbv}$ ). Because the present  
409 photochemical mechanism contains the interconversion of nitrogen oxides (i.e.  
410  $\text{NO}_x=\text{NO}+\text{NO}_2$ ) and oxidants (i.e.  $\text{OX}=\text{NO}_2+\text{O}_3$ ), The following discussions  
411 (subsection 5.2 and 5.3) concentrate more on  $\text{NO}_2$  to simplify analysis. Moreover,  
412 passive dispersion (without chemical reactions, P-type) are also presented to  
413 investigate the sole role of turbulent mixing.

414

### 415 **5.2.1 $\text{NO}_2$ concentration distribution in 3D urban-like models**

416 Fig. 9a-d exhibit  $\text{NO}_2$  concentration between P-type (passive, left) and R-type  
417 (reactive, right) cases in  $y=30\text{m}$  and  $z=1.5\text{m}$  for Street 3 and 10 fixed with span-wise  
418 sources (i.e. S3 and S10). Moreover, Fig. 9e compares  $\text{NO}_2$  concentration at the

419 pedestrian level between passive and reactive cases with  $\text{NO}_x$  sources along main  
420 streets (i.e.  $S_m$ ). For passive dispersion with S3 or S10 sources (P-type), due to source  
421 emissions and turbulent transports,  $\text{NO}_2$  concentration near the upwind building (No.3  
422 and 10) is higher than that near the downwind building(Fig. 9a-b). Furthermore, a  
423 large amount of  $\text{NO}_2$  pollutants accumulate in the intersection of main street and  
424 secondary street(Fig. 9c-d). In an overall view,  $\text{NO}_2$  concentration in Street 10 is  
425 slightly higher than Street 3. For P-type case with  $S_m$  sources(Fig. 9e),  $\text{NO}_2$   
426 concentration first rises toward downstream streets, then reaches an approximate  
427 equilibrium from Street 7 to 18. Such findings are similar with the flow adjustment as  
428 discussed in subsection 5.1.

429 With chemical reactions, as verified by Fig. 9,  $\text{NO}_2$  concentration in R-type cases  
430 considerably exceeds that in P-type cases. Oppositely, passive NO concentration is  
431 higher than that in R-type cases.

432

### 433 5.2.2 $d_{ps}$ distribution in Street 3 and 10

434 Fig. 10 shows  $d_{ps}$  distribution in  $y=30\text{m}$  and  $z=1.5\text{m}$  in local target streets with  
435 S3 and S10 sources. Here, the distribution of photostationary state defect( $d_{ps}$ ) is  
436 emphasized below the roof level ( $z/H<1$ ) and toward downstream domains (i.e.  $x/H>5$   
437 and  $x/H>19$  for Street 3 and 10, respectively).

438 As introduced in subsection 2.2, smaller  $d_{ps}$  value represents the less departure  
439 degree from photochemical equilibrium. In the centre plane of secondary streets

440 ( $y=30\text{m}$ , Fig. 10a), the local small  $d_{ps}$  values emerge near the roof of the upwind  
441 building (No.3 and 10) while the large  $d_{ps}$  values appear near the roof of the  
442 downwind building (No.4 and 11) and the ground level close to  $\text{NO}_x$  emissions. At the  
443 pedestrian level(Fig. 10b), downstream areas of the main streets ( $x/H>6$  and  $x/H>20$ )  
444 experience small  $d_{ps}$  values while the junction regions of the main street and  
445 secondary street near  $\text{NO}_x$  source locations obtain large  $d_{ps}$  values, particularly in  
446 Street 3. In summary,  $d_{ps}$  value is usually smaller in regions with weaker wind and  
447 turbulence, where reactive pollutants have more time to mix and react.

448

### 449 **5.2.3 Concentration, $\langle P_{iF} \rangle_w$ and $\langle P_{iF} \rangle_B$ on building wall surfaces**

450 Based on spatial mean concentration at the entire building surfaces, we calculate  
451 wall intake fraction( $\langle P_{iF} \rangle_w$ ) and building intake fraction( $\langle P_{iF} \rangle_B$ ) to analyze  
452 overall vehicular pollutant( $\text{NO}_x$ ) exposure in near-road buildings. Especially, 1ppm  
453 represents 1 mg inhaled averagely by each person living in the near-road building if  
454 1kg pollutants emitted out.

455 Fig. 11a-b first compare  $\text{NO}_2$  concentration on the leeward and windward walls  
456 between P-type and R-type cases in target street units with S3 and S10 sources. No  
457 matter with or without chemical reactions,  $\text{NO}_2$  concentrations on the leeward wall  
458 are always higher than those on the windward wall. Once  $\text{NO}_x\text{-O}_3$  photochemical  
459 reactions are conducted, an increase of  $\text{NO}_2$  concentration emerges on the upwind and  
460 downwind walls. Such results are similar with the aforementioned discussion in

461 subsection 5.2.1.

462 Then, Table 4 lists  $\langle P_{iF} \rangle_w$  of NO and NO<sub>2</sub> at leeward and windward walls  
463 adjoining target street in cases with S3 and S10 (positions as described in Fig. 3a-b).  
464 Obviously, in both P-type and R-type cases,  $\langle P_{iF} \rangle_w$  of NO<sub>x</sub> at leeward wall (Table 4,  
465 row 1-4, column 2-3) are greater than those at windward wall (Table 4, row 1-4,  
466 column 4-5). Regarding P-type cases as the references,  $\langle P_{iF} \rangle_w$  of NO<sub>2</sub> in R-type  
467 cases rise nearly 90%-160%, i.e. 0.660 to 1.372ppm and 0.853 to 1.643ppm at  
468 leeward wall for S3 and S10 (Table 4, column 2), 0.180 to 0.473ppm and 0.230 to  
469 0.610ppm at windward wall for S3 and S10 (Table 4, column 4); while  $\langle P_{iF} \rangle_w$  of  
470 NO reduces about 9%-16%, i.e. 0.660 to 0.588ppm and 0.853 to 0.775ppm at leeward  
471 wall for S3 and S10 (Table 4, column 3), 0.180 to 0.151ppm and 0.230 to 0.193ppm at  
472 windward wall for S3 and S10 (Table 4, column 5). Because NO<sub>x</sub> emission ratio  
473 released from vehicles is  $R_{NO/NO_2}=10$ , the present photochemical processes lead to a  
474 significant increase in NO<sub>2</sub> exposure and a slight decrease in NO exposure.

475 Furthermore, NO<sub>2</sub> concentrations on the entire building wall surfaces with Sm  
476 sources are presented in Fig. 11c. Both P-type and R-type cases experience the NO<sub>2</sub>  
477 concentration adjustment processes toward downstream buildings. To quantify NO<sub>x</sub>  
478 exposure adjustments in P-type and R-type cases with various sources (S3, S10 and  
479 Sm), the horizontal profiles of building intake fraction  $\langle P_{iF} \rangle_B$  of NO and NO<sub>2</sub> are  
480 shown in Fig. 12. It is found that  $\langle P_{iF} \rangle_B$  with S3 or S10 sources descends  
481 exponentially toward downstream buildings (Fig. 12a-b), instead,  $\langle P_{iF} \rangle_B$  with Sm  
482 sources first ascends quickly from building No.1 to 8, then reaches an approximate

483 equilibrium(Fig. 12c). Besides, R-type cases experience larger NO<sub>2</sub> exposure than  
 484 P-type cases, i.e. 0.420-0.108ppm against 0.135-0.020ppm for S3(Fig. 12a),  
 485 0.605-0.160ppm against 0.207-0.030ppm for S10(Fig. 12b), 0.005-0.090ppm against  
 486 0.002-0.049ppm for Sm(Fig. 12c). Oppositely, NO exposure in P-type cases are  
 487 greater than R-type cases, i.e. 0.135-0.020ppm than 0.106-0.010ppm for S3(Fig. 12a),  
 488 0.207-0.030ppm than 0.168-0.017ppm for S10(Fig. 12b) and 0.002-0.049ppm than  
 489 0.002-0.045ppm for Sm(Fig. 12c).

490 In addition, the decay function expressed in  $\langle P_{iF}_n \rangle_B = a \times \langle P_{iF}_t \rangle_B \times e^{(t-n)/b}$  is  
 491 employed to further quantify the  $\langle P_{iF} \rangle_B$  decay processes from target building unit ( $t$   
 492 =4 or 11) toward downstream building ( $n=t$  to 21) in S3 and S10 cases. Note that,  
 493 smaller decay factor  $b$  means relatively sharper descending processes of  $\langle P_{iF} \rangle_B$   
 494 curves. Table 5 summarizes the  $\langle P_{iF}_t \rangle_B$  of building “No. $t$ ” and the exponential  
 495 decay factors  $b$  in S3 and S10 cases. Obviously, compared with those in P-type case  
 496 ( $b=7.46$  and  $3.96$  in Table 5, row 1 and 3), R-type cases with S3 and S10 obtain larger  
 497  $b$  for NO<sub>2</sub> ( $10.80$  and  $6.84$  in Table 5, row 2 and 4) and smaller  $b$  for NO ( $5.92$  and  
 498  $2.91$ ). Moreover,  $\langle P_{iF} \rangle_B$  curves in S10 cases(Table 5, row 3-4) decline more  
 499 sharply toward downstream regions than S3 cases(Table 5, row 1-2). Particularly, as  
 500 shown in Fig. 12c,  $\langle P_{iF}_t \rangle_B$  in Sm cases are calculated by the mean  $\langle P_{iF} \rangle_B$  from  
 501 building No.9 to 21, i.e. 0.048ppm in P-type case, 0.044ppm and 0.088ppm in R-type  
 502 case for NO and NO<sub>2</sub>.

503 In summary, with  $R_{NO/NO_2}=100:10$  and  $[O_3]=20$ ppbv, the present NO<sub>x</sub>-O<sub>3</sub>  
 504 titration interactions result in the production of NO<sub>2</sub> and depletion of O<sub>3</sub> and NO. By

505 focusing on  $\langle P_{iF} \rangle_B$  values, NO<sub>2</sub> exposure in R-type cases are greater than P-type  
506 cases about 3.1 times for S3, 2.9 times for S10 and 1.8 times for Sm while NO  
507 exposure in R-type cases are nearly 21%, 19% and 8% smaller than P-type cases for  
508 S3, S10 and Sm, respectively.

509

### 510 **5.3 Impacts of reactant proportions (NO:NO<sub>2</sub>:O<sub>3</sub>) on reactive pollutant dispersion**

511 In this subsection, based on S10 sources, we discuss the effects of different  
512 reactant proportions (NO:NO<sub>2</sub>:O<sub>3</sub>) on the interaction of turbulent mixing and  
513 photochemical processes in urban districts. Additionally,  $P_{iF}$  and  $\langle P_{iF} \rangle$  are  
514 independent on source emission strength in passive pollutant dispersion, therefore  
515 Case P[S10,100:10] is treated as the reference case to compare with the cases with  
516 other reactant proportions.

517

#### 518 **5.3.1 Impacts of O<sub>3</sub> background concentration ([O<sub>3</sub>])**

519 With the same emission ratio of NO to NO<sub>2</sub> (i.e.  $R_{NO/NO_2}=100:10$ ), the impacts of  
520 four O<sub>3</sub> background concentrations (i.e. [O<sub>3</sub>] =1, 20, 40 and 100ppbv) on reactive  
521 pollutant dispersion are examined.

522 It is apparent that the formation of NO by photolyzing NO<sub>2</sub> is slightly dominant in  
523 photochemistry when [O<sub>3</sub>] is 1ppbv. In contrast to the reference values (0.853 and  
524 0.230ppm in [Table 4, row 3](#)),  $\langle P_{iF} \rangle_w$  of NO<sub>2</sub> at the leeward and windward walls

525 slightly decrease(i.e. 0.816 and 0.211ppm in Table 4, row 5) while  $\langle P_{iF} \rangle_w$  of NO  
526 increase a little(i.e. 0.858 and 0.233ppm). Besides, such phenomenon is distinctly  
527 observed in  $\langle P_{iF} \rangle_B$  curves(Fig. 13) between the reference case and Case R  
528 [S10,100:10,1], i.e. 0.207-0.030ppm against 0.187-0.020ppm for NO<sub>2</sub>(Fig. 13a) and  
529 0.207-0.030ppm against 0.209-0.031ppm for NO(Fig. 13b).

530 However, if [O<sub>3</sub>] rises from 20ppbv to 40 and 100ppbv, more NO is oxidized by  
531 O<sub>3</sub> to generate NO<sub>2</sub>. Based on the reference values (0.853 and 0.230ppm in Table 4,  
532 row 3),  $\langle P_{iF} \rangle_w$  of NO<sub>2</sub> become about 1.9-5.2 times greater (1.643, 2.454 and  
533 4.442ppm in Table 4, column 2) at leeward wall and 2.6-6.7 times larger (0.610, 0.944  
534 and 1.534ppm in Table 4, column 4) at windward wall; while  $\langle P_{iF} \rangle_w$  of NO  
535 reduces approximately 9%-42% (0.775, 0.694 and 0.495ppm in Table 4, column 3) at  
536 leeward wall and 16%-57% (0.193, 0.159 and 0.100ppm in Table 4, column 5) at  
537 windward wall. Furthermore, Fig. 13 and Table 5 display the corresponding  $\langle P_{iF} \rangle_B$   
538 curves,  $\langle P_{iF} \rangle_B$  values and decay factors  $b$  under different [O<sub>3</sub>]. As depicted in Fig.  
539 13, compared with Case R[S10,100:10,20], Case R[S10,100:10,100] and R  
540 [S10,100:10,40] obviously attain much larger  $\langle P_{iF} \rangle_B$  of NO<sub>2</sub> (1.573-0.275 and  
541 0.952-0.218ppm in Fig. 13a) and smaller  $\langle P_{iF} \rangle_B$  of NO (0.071-0.005 and  
542 0.133-0.011ppm in Fig. 13b). Additionally, both decay factors of NO<sub>2</sub> and NO are  
543 smaller ( $b=6.02$  and  $2.33$  for [O<sub>3</sub>]=40ppbv,  $b=4.74$  and  $1.87$  for [O<sub>3</sub>]=100ppbv in  
544 Table 5, row 6-7) than those in Case R[S10,100:10,20] ( $b=6.84$  and  $2.91$  in Table 5,  
545 row 4), which implies higher [O<sub>3</sub>] induces the quicker decay of  $\langle P_{iF} \rangle_B$  curves for  
546 NO<sub>x</sub> with S10 sources toward downstream building units. By concentrating on

547  $\langle P_{iF} \rangle_B$ , NO<sub>2</sub> exposure in R-type cases surpass the reference case nearly 2.9, 4.6 and  
548 7.6 times for [O<sub>3</sub>]=20, 40 and 100ppbv, respectively (Table 5, column 2).  
549 Correspondingly,  $\langle P_{iF} \rangle_B$  of NO in these [O<sub>3</sub>] cases are about 19%, 36% and 66%  
550 smaller than the reference values, respectively (Table 5, column 4). It clearly indicates  
551 that increasing [O<sub>3</sub>] would aggravate NO<sub>2</sub> exposure within urban clusters but is  
552 conducive to the mitigation of NO exposure.

553

### 554 **5.3.2 Effects of emission ratio of NO to NO<sub>2</sub> ( $R_{NO/NO_2}$ )**

555 The effects of source emission ratios ( $R_{NO/NO_2}$ =100:10, 50:10 and 100:20) on  
556 reactive pollutant dispersion are investigated with the same [O<sub>3</sub>] of 20ppbv.

557 It is shown that decreasing NO or increasing NO<sub>2</sub> emissions based on the  
558 reference case can mildly change the fraction of NO converting into NO<sub>2</sub>. For  
559 example, reducing  $R_{NO/NO_2}$  from 100:10 to 50:10 and 100:20,  $\langle P_{iF} \rangle_w$  of NO  
560 varies from 0.775 to 0.744 and 0.784ppm at the leeward wall (Table 4, column 3), and  
561 from 0.193 to 0.186 and 0.197ppm at windward wall (Table 4, column 5). Furthermore,  
562  $\langle P_{iF} \rangle_w$  of NO<sub>2</sub> drops from 1.643 to 1.406 and 1.205ppm at the leeward wall (Table  
563 4, column 1), and from 0.610 to 0.453 and 0.400ppm at windward wall (Table 4,  
564 column 4). In addition, Fig. 14 presents  $\langle P_{iF} \rangle_B$  curves of NO<sub>2</sub> and NO in P-type and  
565 R-type cases with three NO-NO<sub>2</sub> emission ratios. Obviously, photochemical reactions  
566 in these R-type cases are still dominated by the depletion of O<sub>3</sub> with NO to produce  
567 NO<sub>2</sub>.

568 As displayed in Fig. 14a and Table 5, Case R[S10,50:10,20] and R  
569 [S10,100:20,20] obtain smaller  $\langle P_{iF} \rangle_B$  and decay factor of NO<sub>2</sub> (i.e. 0.446-0.091  
570 ppm,  $b=5.41$  and 0.384-0.088ppm,  $b=6.00$ ) than those in Case R[S10,100:10,20] (i.e.  
571 0.605-0.160ppm,  $b=6.84$ ). In contrast to Case R[S10,100:10,20],  $\langle P_{iF} \rangle_B$  of NO in  
572 Case R[S10,50:10,20] and R[S10,100:20,20] reduce nearly 26% and 37%. However,  
573  $\langle P_{iF} \rangle_B$  curves and decay factors  $b$  of NO are quite close between three R-type cases,  
574 i.e. 0.172-0.018, 0.168-0.018 and 0.160-0.017ppm;  $b=3.05$ , 2.91 and 3.11(Fig. 14b  
575 and Table 5). It is confirmed that the decrement of  $R_{NO/NO_2}$  (from 10 to 5) can partly  
576 offset NO<sub>2</sub> exposure but have much less impacts on NO exposure.

577 Overall, the NO<sub>x</sub>-O<sub>3</sub> photochemical processes dependent on the initial proportion  
578 of reactive pollutants are toward satisfying the photostationary state relationship  
579 (i.e.  $k_f[NO][O_3]=J_{NO_2}[NO_2]$ ).

580

#### 581 **5.4 Limitations and future work**

582 Since the 3D urban district models, photochemical reactions and meteorological  
583 conditions adopted in this study are fairly simplified, the present exposure results may  
584 change if more realistic factors are taken into account, such as more realistic urban  
585 configurations(e.g. with variations of building height and street width), more  
586 complicated chemical mechanisms(e.g. VOCs-NO<sub>x</sub>-O<sub>3</sub>) and more realistic  
587 atmospheric conditions etc. It is worth mentioning that the chemical processes  
588 dependent on reaction rates are highly associated with the reactive pollutant

589 concentration and ambient air temperature. Moreover, realistic atmospheric conditions  
590 include the unsteady temporal and spatial variations of wind speed and direction as  
591 well as various atmospheric stabilities and solar radiation conditions. Thus, further  
592 unsteady CFD simulations will be performed to examine the integrated impacts of  
593 urban turbulence and solar radiation on reactive pollutant dispersion in 3D urban  
594 districts.

595

## 596 **6 Conclusions**

597 Urban residents in near-road buildings commonly suffer from high exposure risk  
598 of vehicular pollutants in which  $\text{NO}_x$  ( $\text{NO}$  and  $\text{NO}_2$ ) act as primary reactive pollutants.  
599 With satisfactory full-scale CFD validation of flow and pollutant dispersion by  
600 experimental data, this study first focuses on the impact of turbulent transport  
601 combined with  $\text{NO}_x$ - $\text{O}_3$  photochemical reactions on reactive pollutant dispersion in  
602 neighborhood-scale (21-row,  $\sim 1\text{km}$ ) three-dimensional (3D) medium-dense urban  
603 clusters ( $H/W=1$ ,  $\lambda_p=\lambda_f=0.25$ ). Ground-level emission sources of  $\text{NO}$  and  $\text{NO}_2$  are  
604 considered in the presence of background  $\text{O}_3$ . The approaching wind is parallel to the  
605 main streets and perpendicular to the secondary streets. As a start, the influences of  
606 various source locations and reactant proportions ( $\text{NO}:\text{NO}_2:\text{O}_3$ ) on pollutant dispersion  
607 are investigated under neutral meteorological condition. Personal intake fraction  $P_{iF}$ ,  
608 its spatially-averaged values for a building wall ( $\langle P_{iF} \rangle_w$ ) and the entire building  
609 surfaces (i.e. building intake fraction  $\langle P_{iF} \rangle_B$ ) are adopted to quantify pollutant

610 exposure with and without NO-NO<sub>2</sub>-O<sub>3</sub> reactions(i.e. reactive and passive).

611 Some meaningful findings are summarized as below:

612 1) There are flow adjustment processes coupling turbulent mixing and chemical  
613 reactions through urban building clusters(Street 1 to Street 20 toward  
614 downstream).With span-wise sources, the secondary street of Street 10 located in the  
615 fully-developed region(i.e. S10 case) experiences weaker wind and subsequently  
616 greater  $\langle P_{iF} \rangle_B$  than the secondary Street 3 located in the upstream flow-adjustment  
617 region (i.e. S3 case). Consequently, in contrast to S3 case, photostationary state defect  
618 ( $d_{ps}$ ) is smaller in S10 case since reactive pollutants have more time to mix and react  
619 in Street 10.

620 2) With source emission ratios of NO to NO<sub>2</sub> of 10( $R_{NO/NO_2}=100:10$ ) and  
621 background O<sub>3</sub> concentration of 20ppbv( $[O_3]=20ppbv$ ), NO-NO<sub>2</sub>-O<sub>3</sub> photochemistry  
622 leads to production of NO<sub>2</sub> and depletion of O<sub>3</sub> and NO, inducing a significant  
623 increase in NO<sub>2</sub> exposure and a slight decrease in NO exposure when compared to  
624 corresponding passive dispersion which only considers the sole role of turbulent  
625 transport. With span-wise pollutant sources, 3D downward helical flows transport  
626 more NO<sub>x</sub> to the leeward side, inducing much greater leeward-side  $\langle P_{iF} \rangle_w$  than the  
627 windward-side. Moreover, by defining exponential decay function expressed  
628 in  $\langle P_{iF}_n \rangle_B = a \times \langle P_{iF}_t \rangle_B \times e^{(t-n)/b}$ , it is found that  $\langle P_{iF} \rangle_B$  descends exponentially  
629 from target building ( $\langle P_{iF} \rangle_B=0.135ppm$  or  $0.207ppm$ ,  $t=4$  or  $11$  for S3 or S10) to  
630 downstream buildings ( $n=t$  to  $21$ ). Especially,  $\langle P_{iF} \rangle_B$  curves decline more sharply

631 from Street 10 toward downstream than that from Street 3. However, if stream-wise  
632 sources fixed along the main streets,  $\langle P_{iF} \rangle_B$  first ascends quickly from building  
633 No.1 to 8, then reaches approximate equilibrium values of  $\langle P_{iF} \rangle_B =$   
634 0.046-0.049ppm.

635 3) Furthermore, the  $O_3$  background concentration ( $[O_3]$ ) and source emission  
636 ratios of NO to  $NO_2$  ( $R_{NO/NO_2}$ ) are confirmed as key factors on  $NO_x-O_3$  reactive  
637 dispersion. The formation of NO by photolyzing  $NO_2$  is slightly dominant in  
638 photochemistry when  $[O_3]$  is 1ppbv. However, if  $[O_3]$  rises from 20ppbv to 40 and  
639 100ppbv, more NO is oxidized by  $O_3$  to generate  $NO_2$ , which would aggravate  $NO_2$   
640 exposure within urban clusters but is conducive to the mitigation of NO exposure.  
641 Under  $[O_3]$  of 20ppbv, results show that the decrement of  $R_{NO/NO_2}$  from 10 to 5 can  
642 partly offset  $NO_2$  exposure but have much less impacts on NO exposure.

643 Although further investigations are still required to provide practical guidelines,  
644 this paper is one of the first attempts to quantify how reactive pollutant source  
645 locations and reactant proportions influence reactive pollutant exposure in 3D urban  
646 districts, which can present meaningful references for urban planning. The effective  
647 methodologies are proposed for reactive pollutant exposure assessment in more  
648 complicated urban districts with various meteorological conditions and chemical  
649 mechanisms.

650

651 **Acknowledgements**

652 This study was financially supported by National Key R&D Program of China  
653 [2016YFC0202206, 2016YFC0202205 and 2016YFC0202204], the National Science  
654 Fund for Distinguished Young Scholars (No. 41425020) and National Natural Science  
655 Foundation--Outstanding Youth Foundation (No. 41622502), STINT (dnr  
656 CH2017-7271) and the National Natural Science Foundation of China (No.  
657 51811530017 and 41875015).

658

## 659 **References list**

- 660 [1] Fenger, J., 1999. Urban air quality. *Atmos. Environ.* 33(29): 4877-4900.
- 661 [2] Chan, C.K., Yao, X.H., 2008. Air pollution in mega cities in China. *Atmos.*  
662 *Environ.* 42: 1-42.
- 663 [3] Pu, Y.C., Yang, C., 2014. Estimating urban roadside emissions with an  
664 atmospheric dispersion model based on in-field measurements. *Environ. Pollut.*  
665 192: 300-307.
- 666 [4] Luo, Z.W., Li, Y.G., Nazaroff, W.W., 2010. Intake fraction of nonreactive motor  
667 vehicle exhaust in Hong Kong. *Atmos. Environ.* 44: 1913-1918.
- 668 [5] Chen, C., Zhao, B., Zhou, W.T., Jiang, X.Y., Tan, Z.C., 2012. A methodology for  
669 predicting particle penetration factor through cracks of windows and doors for  
670 actual engineering application. *Build. Environ.* 47: 339-348.

- 671 [6] Ji, W.J., Zhao, B., 2015. Estimating mortality derived from indoor exposure to  
672 particles of outdoor origin. PLOS.ONE.10, 0124238.
- 673 [7] Hang, J., Luo, Z.W., Wang, X.M., He, L.J., Wang, B.M., Zhu, W., 2017. The  
674 influence of street layouts and viaduct settings on daily CO exposure and intake  
675 fraction in idealized urban canyons. Environ. Pollut. 220: 72-86.
- 676 [8] Ng, W., Chau, C., 2014. A modeling investigation of the impact of street and  
677 building configurations on personal air pollutant exposure in isolated deep urban  
678 canyons. Sci. Total Environ. 468-469: 429-448.
- 679 [9] He, L.J., Hang, J., Wang X.M., Lin B.R., Li, X.H., Lan, G.D., 2017. Numerical  
680 investigations of flow and passive pollutant exposure in high-rise deep street  
681 canyons with various street aspect ratios and viaduct settings. Sci. Total Environ.  
682 584-585: 189-206.
- 683 [10] Scungio, M., Stabile, L., Rizza, V., Pacitto, A., Russi, A., Buonanno, G., 2018.  
684 Lung cancer risk assessment due to traffic-generated particles exposure in urban  
685 street canyons: A numerical modelling approach. Sci. Total. Environ. 631-632:  
686 1109-1116.
- 687 [11] Gu, Z.L., Zhang, Y.W., Cheng, Y., Lee, S.C., 2011. Effect of uneven building  
688 layout on air flow and pollutant dispersion in non-uniform street canyons. Build.  
689 Environ. 46: 2657-2665.
- 690 [12] Yuan, C., Ng, E., 2012. Building porosity for better urban ventilation in  
691 high-density cities - A computational parametric study. Build. Environ.50:

692 176-189.

693 [13]Blocken, B., Vervoort, R., van Hooff, T.A.J., 2016. Reduction of outdoor  
694 particulate matter concentrations by local removal in semi-enclosed parking  
695 garages: a preliminary case study for Eindhoven city center. *J. Wind Eng. Ind.*  
696 *Aerodyn.* 159: 80-98.

697 [14]Santiago, J.L., Borge, R., Martin, F., de la Paz, D., Martilli, A., Lumbreras, J.,  
698 Sanchez, B., 2017. Evaluation of a CFD-based approach to estimate pollutant  
699 distribution within a real urban canopy by means of passive samplers. *Sci. Total*  
700 *Environ.* 576: 46-58.

701 [15]Wang, W.W., Xu, Y., Ng, E., Raasch, S., 2018. Evaluation of satellite-derived  
702 building height extraction by CFD simulations: A case study of  
703 neighborhood-scale ventilation in Hong Kong. *Landscape. Urban. Plan.* 170:  
704 90-102.

705 [16]Oke, T.R., 1988. Street design and urban canopy layer climate. *Energ. Buildings.*  
706 11: 103-113.

707 [17]Vardoulakis, S., Fisher, B.E.A., Pericleous, K., Gonzalez-Flesca, N., 2003.  
708 Modelling air quality in street canyons: a review. *Atmos. Environ.* 37: 155-182.

709 [18]Fernando, H.J.S., Zajic, D., Di Sabatino, S., Dimitrova, R., Hedquist, B., 2010.  
710 Flow, turbulence, and pollutant dispersion in urban atmospheres. *Phys. Fluids.* 22:  
711 1-20.

- 712 [19]Britter, R.E., Hanna, S.R., 2003. Flow and dispersion in urban areas. *Annu. Rev.*  
713 *Fluid. Mech.* 35: 469-496.
- 714 [20]Di Sabatino, S., Buccolieri, R., Salizzoni, P., 2013. Recent advancements in  
715 numerical modelling of flow and dispersion in urban area: a short review. *Int. J.*  
716 *Environ. Pollut.* 52: 172-191.
- 717 [21]Blocken, B., 2015. Computational fluid dynamics for urban physics: importance,  
718 scales, possibilities, limitations and ten tips and tricks towards accurate and  
719 reliable simulations. *Build. Environ.* 91: 219-245.
- 720 [22]Srebric, J., Heidarinejad, M., Liu, J.Y., 2015. Building neighborhood emerging  
721 properties and their impacts on multi-scale modeling of building energy and  
722 airflows. *Build. Environ.* 91: 246-262.
- 723 [23]Meroney, R.N., 2016. Ten questions concerning hybrid computational/physical  
724 model simulation of wind flow in the built environment. *Build. Environ.* 96:  
725 12-21.
- 726 [24]Toparlar, Y., Blocken, B., Maiheu, B., van Heijst, G.J.F., 2017. A review on the  
727 CFD analysis of urban microclimate. *Renew. Sustain. Energy Rev.* 80:  
728 1613-1640.
- 729 [25]Zhong, J., Cai, X.M., Bloss, W.J., 2016. Coupling dynamics and chemistry in the  
730 air pollution modelling of street canyons: A review. *Environ. Pollut.* 214:  
731 690-704

- 732 [26]Zhang Y.W., Gu Z., Chuck W. Y., 2018. Review on numerical simulation of  
733 airflow and pollutant dispersion in urban street canyons under natural background  
734 wind conditions. *Aerosol. Air. Qual. Res.* 18: 780-789.
- 735 [27]Blocken, B., 2018. LES over RANS in building simulation for outdoor and  
736 indoor applications : A foregone conclusion ? *Build. Simul.* 821-870.
- 737 [28]Lai, D., Liu, W., Gan, T., Liu, K., Chen, Q., 2019. A review of mitigating  
738 strategies to improve the thermal environment and thermal comfort in urban  
739 outdoor spaces. *Sci. Total Environ.* 661: 337-353.
- 740 [29]Li, X., Liu, C.H., Leung, D.Y.C., Lam, K.M., 2006. Recent progress in CFD  
741 modelling of wind field and pollutant transport in street canyons. *Atmos. Environ.*  
742 40: 5640-5658.
- 743 [30]Li, X.X., Liu, C.H., Leung, D.Y.C., 2009. Numerical investigation of pollutant  
744 transport characteristics inside deep urban street canyons. *Atmos. Environ.* 43  
745 (15): 2410-2418.
- 746 [31]Lin, L., Hang, J., Wang, X.X., Wang, X.M., Fan, S.J., Fan, Q., Liu, Y.H., 2016.  
747 Integrated effects of street layouts and wall heating on vehicular pollutant  
748 dispersion and their reentry into downstream canyons. *Aerosol Air Qual. Res.* 16:  
749 3142-3163.
- 750 [32]Ding, S., Huang, Y.D., Cui, P.Y., Wu, J., Li, M.Z., Liu, D.T., 2019. Impact of  
751 viaduct on flow reversion and pollutant dispersion in 2D urban street canyon with

752 different roof shapes -Numerical simulation and wind tunnel experiment. *Sci.*  
753 *Total. Environ.* 671: 976-991.

754 [33]Chang, C.H., Meroney, R.N., 2003. Concentration and flow distributions in urban  
755 street canyons: wind tunnel and computational data. *J. Wind Eng. Ind. Aerodyn.*  
756 91: 1141-1154.

757 [34]Buccolieri, R., Sandberg, M., Di Sabatino, S., 2010. City breathability and its link  
758 to pollutant concentration distribution within urban-like geometries. *Atmos.*  
759 *Environ.* 44: 1894-1903.

760 [35]Hang, J., Li, Y.G., 2011. Age of air and air exchange efficiency in high-rise urban  
761 areas. *Atmos. Environ.* 45 (31): 5572-5585.

762 [36]Yuan, C., Ng, E., Norford, L.K., 2014. Improving air quality in high-density cities  
763 by understanding the relationship between air pollutant dispersion and urban  
764 morphologies. *Build. Environ.* 71: 245-258.

765 [37]Ramponi, R., Blocken, B., de Coo, L.B., Janssen, W.D., 2015. CFD simulation of  
766 outdoor ventilation of generic urban configurations with different urban densities  
767 and equal and unequal street widths. *Build. Environ.* 92: 152-166.

768 [38]Chen, L., Hang, J., Sandberg, M., Claesson, L., Di Sabatino, S., Wigo, H., 2017.  
769 The impacts of building height variations and building packing densities on flow  
770 adjustment and city breathability in idealized urban models. *Build. Environ.* 118:  
771 344-361.

- 772 [39]Hang, J., Li, Y.G., Sandberg, M., Buccolieri, R., Di Sabatino, S., 2012. The  
773 influence of building height variability on pollutant dispersion and pedestrian  
774 ventilation in idealized high-rise urban areas. *Build. Environ.* 56: 346-360.
- 775 [40]Lin, M., Hang, J., Li, Y., Luo, Z., Sandberg, M., 2014. Quantitative ventilation  
776 assessments of idealized urban canopy layers with various urban layouts and the  
777 same building packing density. *Build. Environ.*, 79: 152-167.
- 778 [41]Sha, C.Y., Wang, X.M.,Lin, Y.Y., Fan, Y.F., Chen, X., Hang, J., 2018. The  
779 impact of urban open space and 'lift-up' building design on building intake  
780 fraction and daily pollutant exposure in idealized urban models. *Sci. Total.*  
781 *Environ.* 633: 1314-1328.
- 782 [42]Liu, J.L., Niu, J.L., Mak, C.M., Xia, Q., 2017. Detached eddy simulation of  
783 pedestrian-level wind and gust around an elevated building. *Build. Environ.* 125:  
784 168-179.
- 785 [43]Du, Y.X., Mak, C.M., Liu, J.L., Xia, Q., Niu, J.L., Kwok, K.C.S., 2017. Effects  
786 of lift-up design on pedestrian level wind comfort in different building  
787 configurations under three wind directions. *Build. Environ.* 117: 84-99.
- 788 [44]Zhang, K., Chen, G., Wang, X., Liu, S., Mak, C. M., Fan, Y., Hang, J., 2019.  
789 Numerical evaluations of urban design technique to reduce vehicular personal  
790 intake fraction in deep street canyons. *Sci. Total. Environ.* 653: 968-994.

- 791 [45]Chew, L.W., Nazarian, N., Norford, L., 2017. Pedestrian-level urban wind flow  
792 enhancement with wind catchers. *Atmos.* 8(9): 159 (DOI: 10.3390/  
793 atmos8090159)
- 794 [46]Buccolieri, R., Salim, S.M., Leo, L.S., Di Sabatino, S., Chan, A., Ielpo, P., de  
795 Gennaro, G., Gromke, C., 2011. Analysis of local scale tree-atmosphere  
796 interaction on pollutant concentration in idealized street canyons and application  
797 to a real urban junction. *Atmos. Environ.* 45: 1702-1713.
- 798 [47]Buccolieri, R., Santiago, J.L., Rivas, E., Sanchez, B., 2018. Review on urban tree  
799 modelling in CFD simulations: Aerodynamic, deposition and thermal effects.  
800 *Urban for Urban Gree*, 31: 212-220.
- 801 [48]Gromke, C., Blocken, B., 2015. Influence of avenue-trees on air quality at the  
802 urban neighborhood scale. Part I: quality assurance studies and turbulent Schmidt  
803 number analysis for RANS CFD simulations. *Environ. Pollut.* 196: 214-223.
- 804 [49]Yuan, C., Norford, L., Ng, E., 2017. A semi-empirical model for the effect of  
805 trees on the urban wind environment. *Landscape. Urban. Plan.* 168: 84-93.
- 806 [50]Xie, X.X., Huang, Z., Wang, J.S., 2006. The impact of urban street layout on  
807 local atmospheric environment. *Build. Environ.* 41: 1352-1363.
- 808 [51]Cai, X., 2012. Effects of differential wall heating in street canyons on dispersion  
809 and ventilation characteristics of a passive scalar. *Atmos. Environ.* 51: 268-277.

810 [52]Allegri, J., Dorer, V., Carmeliet, J., 2014. Buoyant flows in street canyons:  
811 Validation of CFD simulations with wind tunnel measurements. *Build. Environ.*  
812 72: 63-74.

813 [53]Yang, X.Y., Li, Y.G., 2015.The impact of building density and building height  
814 heterogeneity on average urban albedo and street surface temperature. *Build.*  
815 *Environ.* 90: 146-156.

816 [54]Liu, J., Heidarinejad, M., Gracik, S., Srebric, J., 2015. The impact of exterior  
817 surface convective heat transfer coefficients on the building energy consumption  
818 in urban neighborhoods with different plan area densities. *Energy Build.* 86: 449–  
819 463.

820 [55]Wang, X.X., Li, Y.G., 2016. Predicting urban heat island circulation using CFD.  
821 *Build. Environ.* 99: 82-97.

822 [56]Fan, Y.F., Hunt, J.C.R., Li, Y.G., 2017. Buoyancy and turbulence-driven  
823 atmospheric circulation over urban areas. *J. Environ. Sci.* 59: 63-71.

824 [57]Lin, Y., Chen, G., Chen, T., Luo, Z., Yuan, C., Gao, P., Hang, J., 2019. The  
825 influence of advertisement boards, street and source layouts on CO dispersion  
826 and building intake fraction in three-dimensional urban-like models. *Build.*  
827 *Environ.* 150: 297-321.

828 [58]Habilomatis, G., Chaloulakou, A., 2015. A CFD modelling study in an urban  
829 street canyon for ultrafine particles and population exposure: the intake fraction  
830 approach. *Sci. Total Environ.* 530-531: 227-232.

- 831 [59] Baker, J., Walker, H.L., Cai, X.M., 2004. A study of the dispersion and transport  
832 of reactive pollutants in and above street canyons - a large eddy simulation.  
833 Atmos. Environ. 38: 6883-6892.
- 834 [60] Baik, J.-J., Kang, Y.-S., Kim, J.-J., 2007. Modeling reactive pollutant dispersion  
835 in an urban street canyon. Atmos. Environ. 41: 934-949.
- 836 [61] Grawe, D., Cai, X.-M., Harrison, R.M., 2007. Large eddy simulation of shading  
837 effects on NO<sub>2</sub> and O<sub>3</sub> concentrations within an idealised street canyon. Atmos.  
838 Environ. 41: 7304-7314.
- 839 [62] Kang, Y.-S., Baik, J.J., Kim, J.J., 2008. Further studies of flow and reactive  
840 pollutant dispersion in a street canyon with bottom heating. Atmos. Environ. 42:  
841 4964-4975.
- 842 [63] Tong, N.Y.O., Leung, D.Y.C., 2012. Effects of building aspect ratio, diurnal  
843 heating scenario, and wind speed on reactive pollutant dispersion in urban street  
844 canyons. J. Environ. Sci.-China 24: 2091-2103.
- 845 [64] Zhong, J., Cai, X.M., Bloss, W.J., 2015. Modelling the dispersion and transport  
846 of reactive pollutants in a deep urban street canyon: using large-eddy simulation.  
847 Environ. Pollut. 200: 42-52.
- 848 [65] Kim, M.J., Park, R.J., Kim, J.J., 2012. Urban air quality modeling with full  
849 O<sub>3</sub>-NO<sub>x</sub>-VOC chemistry: implications for O<sub>3</sub> and PM air quality in a street  
850 canyon. Atmos. Environ. 47: 330-340.

- 851 [66]Park, S.J., Kim, J.J., Kim, M.J., Park, R.J., Cheong, H.-B., 2015. Characteristics  
852 of flow and reactive pollutant dispersion in urban street canyons. *Bound. Layer  
853 Meteorol.* 108: 20-31.
- 854 [67]Garmory, A., Kim, I.S., Britter, R.E., Mastorakos, E., 2009. Simulations of the  
855 dispersion of reactive pollutants in a street canyon, considering different  
856 chemical mechanisms and micromixing. *Atmos. Environ.* 43: 4670-4680.
- 857 [68]Kwak, K.H., Baik, J.J., 2012. A CFD modeling study of the impacts of NO<sub>x</sub> and  
858 VOC emissions on reactive pollutant dispersion in and above a street canyon.  
859 *Atmos. Environ.* 46: 71-80.
- 860 [69]Kwak, K.H., Baik, J.J., Lee, K.Y., 2013. Dispersion and photochemical evolution  
861 of reactive pollutants in street canyons. *Atmos. Environ.* 70: 98-107.
- 862 [70]Allan, M., Richardson, G.M., Jones-Otazo, H., 2008. Probability density  
863 functions describing 24-hour inhalation rates for use in human health risk  
864 assessments: an update and comparison. *Hum. Ecol. Risk Assess.* 14: 372-391.
- 865 [71]Chau, C.K., Tu, E.Y., Chan, D.W.T., Burnett, C.J., 2002. Estimating the total  
866 exposure to air pollutants for different population age groups in Hong Kong.  
867 *Environ. Int.* 27: 617-630.
- 868 [72]Quang, T.N., He, C., Morawska, L., Knibbs, L.D., Falk, M., 2012. Vertical  
869 particle concentration profiles around urban office buildings. *Atmos. Chem. Phys.*  
870 12: 5017-5030.

- 871 [73]Tominaga, Y., Stathopoulos, T., 2013. CFD simulation of near-field pollutant  
872 dispersion in the urban environment: A review of current modeling techniques.  
873 *Atmos. Environ.* 79: 716-730.
- 874 [74]Zhang, Y.W., Gu, Z., Lee, S.C., Fu, T.M., Ho, K.F., 2011. Numerical simulation  
875 and in situ investigation of fine particle dispersion in an actual deep street canyon  
876 in Hong Kong. *Indoor. Built. Environ.* 20: 206-216.
- 877 [75]Salim, S.M., Buccolieri, R., Chan, A., Di Sabatino, S., 2011. Numerical  
878 simulation of atmospheric pollutant dispersion in an urban street canyon:  
879 comparison between RANS and LES. *J. Wind Eng. Ind. Aerodyn.* 99: 103-113.
- 880 [76]Ashie, Y., Kono, T., 2011. Urban-scale CFD analysis in support of a  
881 climate-sensitive design for the Tokyo Bay area. *Int. J. Climatol.* 31: 174-188.
- 882 [77]Panagiotou, I., Neophytou, M.K.A., Hamlyn, D., Britter, R.E., 2013. City  
883 breathability as quantified by the exchange velocity and its spatial variation in  
884 real inhomogeneous urban geometries: An example from central London urban  
885 area. *Sci. Total Environ.* 442: 466-477.
- 886 [78]Hang, J., Wang, Q., Chen, X.Y., Sandberg, M., Zhu, W., Buccolieri, R., Di  
887 Sabatino, S., 2015. City breathability in medium density urban-like geometries  
888 evaluated through the pollutant transport rate and the net escape velocity. *Build.*  
889 *Environ.* 94: 166-182.

- 890 [79]Hang, J., Xian, Z., Wang, D., Mak, C. M., Wang, B., & Fan, Y., 2018. The  
891 impacts of viaduct settings and street aspect ratios on personal intake fraction in  
892 three-dimensional urban-like geometries. *Build. Environ.* 143: 138-162.
- 893 [80]ANSYS Inc, ANSYS FLUENT User's Guide, (Version 15.0).
- 894 [81]Seinfeld, J.H., Pandis, S.N., 1998. *Atmospheric Chemistry and Physics*.  
895 Wiley-Interscience, New York.
- 896 [82]Lien, F.S., Yee, E., 2004. Numerical modeling of the turbulent flow developing  
897 within and over a 3-D building array, part I: A high-resolution  
898 Reynolds-averaged Navier-Stokers approach. *Bound-lay. Meteorol.* 112:  
899 427-466.
- 900 [83]Santiago, J.L., Martilli, A., Martin, F., 2007. CFD simulation of airflow over a  
901 regular array of cubes. Part I: three dimensional simulation of the flow and  
902 validation with wind-tunnel measurements. *Bound-lay. Meteorol.* 122: 609-634.
- 903 [84]Tominaga, Y., Mochida, A., Yoshie, R., Kataoka, H., Nozu, T., Yoshikawa, M.,  
904 Shirasawa T., 2008. AIJ guidelines for practical applications of CFD to pedestrian  
905 wind environment around buildings. *J. Wind Eng. Ind. Aerodyn.* 96: 1749-1761.
- 906 [85]Franke, J., Hellsten, A., Schlünzen, H., Carissimo, B., 2007. Best practice  
907 guideline for the CFD simulation of flows in the urban environment, in: *COST*  
908 *Action 732*. pp. 1-52.
- 909 [86]Franke, J., Hellsten, A., Schlunzen, H., Carissimo, B., 2011. *The COST732 Best*

910 Practice Guideline for CFD simulation of flows in the urban environment a  
911 summary. *Int. J. Environ. Pollut.* 44: 419-427.

912 [87]Brown, M.J., Lawson, R.E., DeCroix, D.S., Lee, R. L., 2001. Comparison of  
913 centerline velocity measurements obtained around 2D and 3D building arrays in a  
914 wind tunnel. Report LA-UR-01-4138, Los Alamos National Laboratory, Los  
915 Alamos, pp.7.

916 [88]Blocken, B., Stathopoulos, T., Carmeliet, J., 2007. CFD simulation of the  
917 atmospheric boundary layer: wall function problems. *Atmos. Environ.* 41: 238–  
918 252.

919 [89]van Hooff, T., Blocken, B., 2013. CFD evaluation of natural ventilation of indoor  
920 environments by the concentration decay method: CO<sub>2</sub> gas dispersion from a  
921 semienclosed stadium. *Build. Environ.* 61: 1–17.

922 [90]Carslaw, D. C., 2005. Evidence of an increasing NO<sub>2</sub>/NO<sub>x</sub> emissions ratio from  
923 road traffic emissions. *Atmos. Environ.* 39(26): 4793-4802.

924 [91]Di Sabatino, S., Buccolieri, R., Olesen, H.R., Ketzler, M., Berkowicz, R., Franke,  
925 J., Schatzmann, M., Schlunzen, K.H., Leitl, B., Britter, R., Borrego, C., Costa,  
926 A.M., Trini Castelli, A., Reisin, T.G., Hellsten, A., Saloranta, J., Moussiopoulos,  
927 N., Barmpas, F., Brzozowski, K., Goricsan, I., Balczo, M., Bartzis, J.G.,  
928 Efthimiou, G., Santiago, J.L., Martilli, A., Piringer, M., Baumann-Stanzer, K.,  
929 Hirtl, M., Baklanov, A.A., Nuterman, R.B., Starchenko, A.V., 2011. COST 732  
930 in practice: the MUST model evaluation exercise. *Int. J. Env. Poll.*44 (1/2/3/4).

931 [92]Chang, C. H., Meroney, R. N., 2001. Numerical and physical modeling of bluff  
932 body flow and dispersion in urban street canyons. J. Wind Eng. Ind. Aerodyn. 89  
933 (14-15): 1325-1334.

934 [93]Irwin, J.S., 1979. A theoretical variation of the wind profile power-law exponent  
935 as a function of surface roughness and stability. Atmos. Environ. 13(1):191-194.

936

937 **Figure list:**

938 Fig.1 (a) The population census data of Hong Kong [4]; (b) Time activity patterns for  
939 each subgroup in four microenvironments [70].

940 Fig.2 (a) Idealized 3D urban district models ( $H/W=1$ ,  $\lambda_p=\lambda_f=0.25$ ); (b)  
941 Computational domains and boundary conditions for test cases; (c) The overhead  
942 and lateral views of mesh distribution.

943 Fig.3 Model setups of vehicular emission sources: (a) S3, (b) S10 and (c) Sm.

944 Fig.4 (a-b) The side and top views of measured points and model configurations in  
945 wind tunnel experiment [87]; (c) Computational domains and boundary  
946 conditions in CFD validation study; (d) The mesh arrangements in grid  
947 sensitivity test.

948 Fig.5 Results of grid independence test: (a)  $\bar{u}(z)$ , (b)  $\bar{w}(z)$  at Point V1; Comparison of  
949 vertical profiles between wind tunnel data and CFD results: (c-e)  $\bar{u}(z)$  at Points  
950 V1, V4 and V6, respectively; (f-g)  $\bar{w}(z)$  and  $k(z)$  at Point V1.

951 Fig.6 (a-b) The lateral and overhead views of experiment settings in concentration  
952 measurement [92]; (c) CFD setups in passive dispersion validation; (d-f) Vertical  
953 profiles of stream-wise velocity, turbulence kinetic energy and turbulent  
954 dissipation rate in domain inlet.

955 Fig.7 Comparison of  $K$  between wind tunnel data and CFD results applying standard  
956  $k-\varepsilon$  model: (a) on the leeward and windward walls; (b) on the central line of roof  
957 surface.

958 Fig.8 (a) Velocity distribution in the pedestrian level of  $z=1.5\text{m}$ ; (b-c) Velocity  
959 magnitude and 2D streamlines for Street 3 (left) and 10 (right) in the plane of  
960  $y=30\text{m}$  and  $z=1.5\text{m}$ , respectively; (d) 3D streamlines in Street 3 and 10.

961 Fig.9  $\text{NO}_2$  concentration distribution between P-type (left or above) and R-type (right  
962 or below) cases: (a-b) in the plane of  $y=30\text{m}$  with S3 and S10, respectively; (c-d)  
963 in the pedestrian level of  $z=1.5\text{m}$  with S3 and S10, respectively; (e) in the  
964 pedestrian level of  $z=1.5\text{m}$  with Sm.

965 Fig.10 (a-b) Photostationary state defect between S3 (left) and S10 (right) cases in  
966  $y=30\text{m}$  and  $z=1.5\text{m}$ , respectively.

967 Fig. 11  $\text{NO}_2$  concentration between P-type (left or above) and R-type (right or below)  
968 cases: (a-b) on the leeward and windward walls with S3 and S10, respectively; (c)  
969 on the entire building walls with Sm.

970 Fig.12  $\langle P_{iF} \rangle_B$  curves of NO and  $\text{NO}_2$  in P-type and R-type cases with various  
971 source locations: (a) S3, (b) S10 and (c) Sm, respectively.

972 Fig. 13  $\langle P_{iF} \rangle_B$  curves of (a) NO<sub>2</sub> and (b) NO in P-type and R-type cases under four  
973 O<sub>3</sub> background concentrations ([O<sub>3</sub>]=1,20,40,100ppbv).

974 Fig. 14  $\langle P_{iF} \rangle_B$  curves of (a) NO<sub>2</sub> and (b) NO in P-type and R-type cases with three  
975 kinds of NO-NO<sub>2</sub> emission ratios.

976

977 **Table list:**

978 Table 1 Time patterns and breathing rates in each subgroup for indoors at home ( $j=1$ )

979 Table 2 Summary of all test cases

980 Table 3 Comparison between wind tunnel experiment and CFD simulation

981 Table 4  $\langle P_{iF} \rangle_W$  (unit: ppm) at leeward and windward walls adjoining the target  
982 street in S3 and S10 cases

983 Table 5  $\langle P_{iF} \rangle_B$  values and the exponential factor  $b$  in S3 and S10 cases

984